Application of acoustic noise and self-potential localization techniques to a buried hydrothermal vent (Waimangu Old Geyser site, New Zealand)

J. Vandemeulebrouck, P. Roux, P. Gouédard, A. Legaz, A. Revil, A.W. Hurst, A. Bolève, Abderrahim Jardani

Geophysical Journal International

Geophys. J. Int. (2010) **180,** 883–890 doi: 10.1111/j.1365-246X.2009.04454.x

Application of acoustic noise and self-potential localization techniques to a buried hydrothermal vent (Waimangu Old Geyser site, New Zealand)

J. Vandemeulebrouck,[1] P. Roux,[2] P. Gouédard,[2] A. Legaz,[1] A. Revil,[1,3] A.W. Hurst,[4] A. Bolève[1] and A. Jardani[3,5]

[1]*LGIT, CNRS, Université de Savoie, Chambéry, France. E-mail: jvand@univ-savoie.fr*
[2]*LGIT, CNRS, Université Joseph Fourier, Grenoble, France*
[3]*Department of Geophysics, Colorado School of Mines, Golden, CO, USA*
[4]*Institute of Geological and Nuclear Sciences, Lower Hutt, New Zealand*
[5]*M2C, CNRS, Université de Rouen, Mont Saint Aignan, France*

Accepted 2009 November 11. Received 2009 November 6; in original form 2008 September 18

SUMMARY

A seismo-acoustic and self-potential survey has been performed in the hydrothermal area of the old Waimangu Geyser (New Zealand), which was violently erupting a century ago. Nowadays, no surface activity is visible there. We set-up an array of 16 geophones and recorded a high and steady acoustic ambient noise. We applied the matched field processing (MFP) approach to the acoustic data to locate the sources responsible for the ambient noise. The white noise constraint processor reveals the presence of a unique and well-focused acoustic source at a depth of 1.5 m below the seismic array. For this very shallow source, the application of MFP enabled the determination of both the source location and the dispersion curve of seismic velocity. The study was completed by self-potential (SP) measurements on several profiles around the acoustic noise source, which displayed a large positive anomaly above it. The results of the SP inversion gave an electric streaming current density source very close to the acoustic one. Both sources likely belong to a shallow hydrothermal structure interpreted as a small convective cell of boiling water beneath an impermeable layer. The joint application of these methods is a promising technique to recognize hydrothermal structures and to study their dynamics.

Key word: Tomography; Hydrogeophysics; Hydrothermal systems; Volcano seismology; Wave propagation; New Zealand.

1 INTRODUCTION

The Waimangu valley, located in the North Island of New Zealand, is a recent hydrothermal site in the Taupo Volcanic Zone (TVZ). Prior to the 1886 eruption of Mt. Tarawera volcano, surface activity was restricted to the world famous Pink and White Terraces near Lake Rotomahana. During the 1886 eruption, a series of craters opened along a length of 17 km, with Waimangu at the southwestern end (Nairn & Cole 1981). After the eruption, the Waimangu hydrothermal features (Fig. 1) developed in some of the 1886 craters (Scott 1994). In 1900, the Waimangu geyser started to erupt in the eastern part of Echo Crater (Fig. 1), and continued until 1904. Its eruption height was remarkable, up to 450 m (Keam 1980), making Waimangu the world's highest historical geyser, and its cycle period was about 36 hr. During the following years, many hydrothermal eruptions occurred in Echo Crater, with the largest on April 1917. This eruption covered the site of the Geyser and re-excavated the western part of Echo Crater, now filled by Frying Pan Lake.

At present, the Waimangu main surface activity is located in and around Frying Pan and Inferno Lakes (Fig. 1), which present a cyclic activity with level and temperature changes (Scott 1994). The site occupied previously by Waimangu Geyser is an almost flat area, covered by altered deposits of hydrothermal eruptions, where surface activity can only be observed in the northern part with a small boiling pool. Water flow coming from the direction of the Geyser site can be seen when it joins the Frying Pan outlet stream.

Tosha *et al.* (1996) recorded the seismic noise activity in Waimangu and observed a continuous background signal in this area, with a stronger signal when the Inferno water level was rising. The source of these hydrothermal noise variations can be attributed to boiling instabilities at depth (Vandemeulebrouck *et al.* 2005). Tosha *et al.* (1996) monitored the self-potential changes on an east–west profile and observed a positive anomaly centred on the Geyser site, attributed to subsurface upflow, whose amplitude changed with time during the Inferno cycle.

This paper aims to study the structure of this area (now known as the Old Geyser site), which represents a remarkable source of

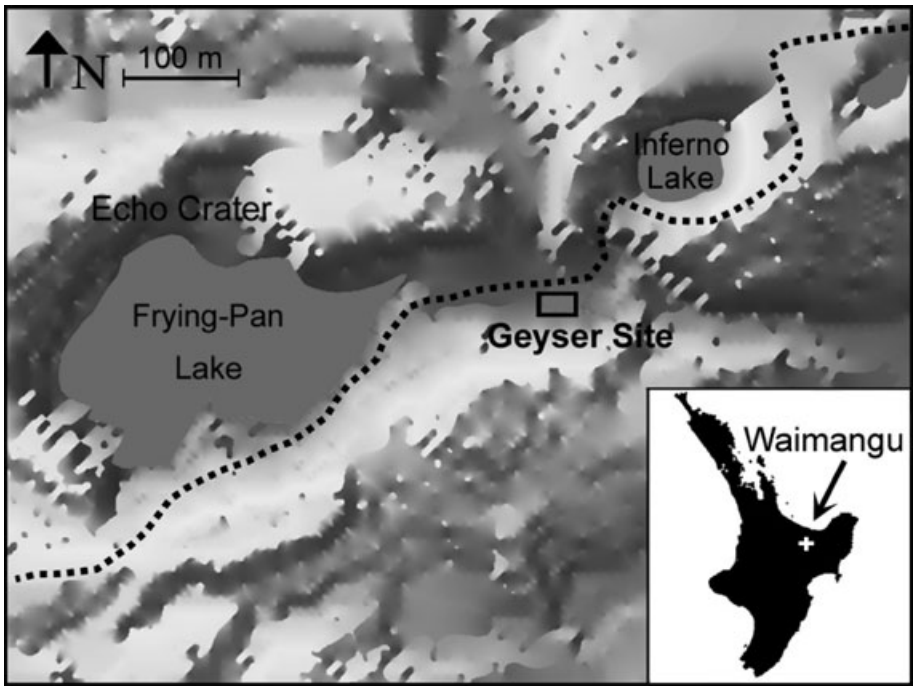

Figure 1. Map of Waimangu hydrothermal area in the North Island of New Zealand. The rectangle corresponds to the location of the acoustic and self-potential survey at the Old Geyser site.

correlated acoustic noise and electric self-potential. The combination of different geophysics methods on hydrothermal systems has improved the knowledge of their structural features (Aizawa *et al.* 2005; Bruno *et al.* 2007). Self-potential data have been recently combined with temperature and CO_2 measurements to better constrain the heat, gas and water flows inside Mt. Vulcano (Revil *et al.* 2008). The use of resistivity tomography is very useful for the recognition of geothermal structures (e.g. Bibby *et al.* 1994), but is also necessary for a complete inversion of self-potential data to assess water circulation in complex volcanic structures (Jardani *et al.* 2008). To the best of our knowledge, this is the first time ambient acoustic noise measurements and self-potential data have been used together on a geothermal area. Both methods are related to dynamic processes inside the hydrothermal system: acoustic energy is produced by boiling and cavitation (Leet 1988), and electric potential is generated by groundwater flow. The combination of these methods is likely to provide better information on the underground structure and the physical processes occurring there.

2 DESCRIPTION OF SURVEY AND METHODS

2.1 Seismo-acoustic experiments and method

The goal of the seismo-acoustic experiment was to analyse the ambient hydrothermal noise at the Old Geyser site area, during a period of Inferno Lake stability. The acoustic method we propose is original for the recognition of hydrothermal dynamic structures, as (1) it applies to ambient noise and not to discrete events (e.g. Almendros *et al.* 2001) and (2) it uses localization methods developed in ocean acoustics. Indeed, recent papers on noise correlation techniques have demonstrated the spatial coherence of ambient seismic noise on length scales varying from hundreds of metres to hundreds of kilometres and frequencies between 0.1 and 1 Hz (Roux *et al.* 2005; Shapiro *et al.* 2005; Brenguier *et al.* 2008). Hydrothermal

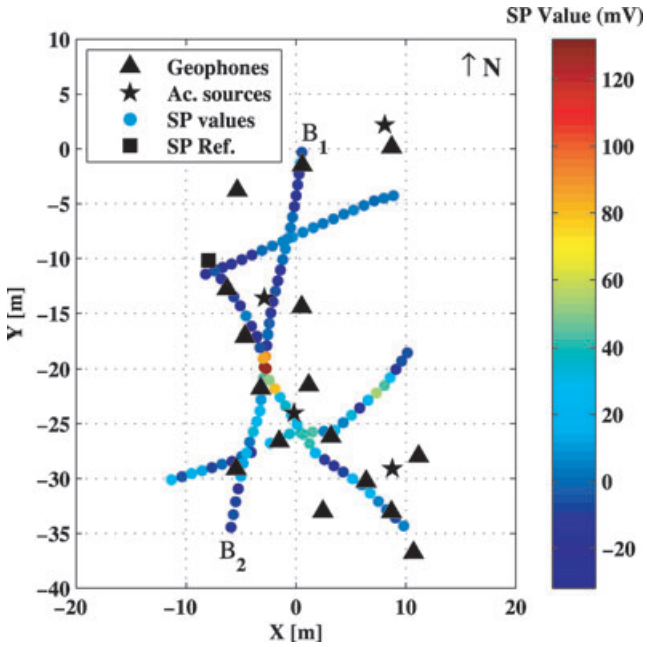

Figure 2. Map showing the location of geophones (black triangles) array and artificial acoustic sources (black stars) over the studied area. The self-potential variations measured on the four profiles are represented by circles of different colours; see the colour bar for corresponding values in mV. The SP reference point is indicated as a black square.

systems classically generate seismic noise above 10 Hz (Kieffer 1984), which is clearly coherent on geophone arrays with inter-element distances smaller than 50 m (Legaz *et al.* 2009a). Our goal is to take advantage of this spatial coherence to perform coherent array processing to localize the sources of hydrothermal noise.

We set up at the Old Geyser site an array of sixteen 4.5 Hz vertical geophones (black triangles in Fig. 2). All the seismic channels were

synchronized and data were recorded on a laptop using a 12-bit resolution data acquisition board. To constrain the seismic velocity c of the area, we first performed four series of active experiments using the method of Gouedard *et al*. (2008). It consisted in recording the seismic signal produced by several people stepping in a small area, about 1 m in diameter, at reference points on different sides of the array (black stars in Fig. 2). We then applied matched field processing (MFP) techniques, as described later, to localize the artificial sources, although interactively changing the velocity. We found a value for c, about 160 ms^{-1} in the [15–30 Hz] bandwidth, which gives consistent locations for all the active experiment spots, and we considered the velocity as homogeneous in the studied domain. The low value of c means that the vertical component of the seismic field recorded on the geophone array is dominated by surface waves. Furthermore, the value of c shows that the extent of the geophone array covers a few acoustic wavelengths, which is a requisite for source localization using phase-matching techniques.

We then recorded the ambient seismic noise during several intervals, each 4 min long, at a sampling rate of 800 Hz. Fig. 3 shows a time–frequency spectrogram of 2 min of seismic noise recorded on one geophone. The ambient noise looks Gaussian in the time domain with seismic energy distributed between 6 and 35 Hz. To localize in depth and range the ambient noise sources, we applied the MFP technique, commonly used in ocean acoustics (Jensen *et al.* 1994). MFP is an array-processing technique based on comparing forward modelling solutions of the wave equation with acquired data, measured on an array of motion sensors. MFP consists in placing a test source at each point of a search grid, computing the acoustic field (replicas) at all the P elements of the array, and then correlating this modelled field with the data from the real point source, whose location is unknown. First, we consider several (N) time segments in the record and transform the acoustic signal in the frequency domain $d_{i,k}(\omega)$, where i refers to the array element number ($i \in [1, P]$), k is the time segment number ($k \in [1, N]$) and ω is the frequency. We then create the cross-spectral density matrix (CSDM) K_{ij} ($i, j \in [1, P]$) through an ensemble average performed on N temporal segments of the data vector

$$K_{ij}(\omega) = \frac{1}{N} \sum_{k=1}^{N} d_{i,k}(\omega)\, d^{*}_{j,k}(\omega). \tag{1}$$

The star stands for the complex conjugate transpose operation. Practically speaking, N is always chosen to be larger than the number of sensors so that the CSDM is a full-rank matrix (Jensen *et al.* 1994). The CSDM is the acoustic equivalent of the cross power spectrum CPS that has been used by several authors in surface wave seismology (Asten & Henstridge 1984; Horike 1985; Zywicki 1999; Foti 2000). Then, the matched field processor (called Bartlett processor) is applied through the following estimator:

$$B(a) = \sum_{\omega} |\tilde{d}^{*}(\omega, a) K(\omega) \tilde{d}(\omega, a)|, \tag{2}$$

where a is a P-element vector corresponding to the absolute distance between the source candidate position in the medium and each of the array element. The P-element replica vector $\tilde{d}(\omega, a)$ is defined as the free-space Green's function at frequency ω from a candidate source position to the array elements. We have

$$\tilde{d}(\omega, a) = \frac{1}{4\pi a} \exp\left(j \frac{\omega a}{c}\right), \tag{3}$$

where B is the equivalent of a linear 'correlator', for which the correlation is maximum when the candidate point source is colocated with the true point source. The matched-field processor B is incoherently averaged over the frequency bandwidth of interest to further improve the contrast of the ambiguity surface. In eq. (3), we chose the free-space monopolar Green's function since we expect to retrieve a local source for which the geophones array is located in the near field (at most one or two wavelengths away from the source). In the near field of the source, the separation between Rayleigh wave and body wave is not yet effective. In this case, wave propagation can be characterized by a velocity c that depends on the density and the bulk modulus of the medium.

The central difficulty of MFP is the knowledge of the environment, to generate the proper replica vectors. Depending on the expected mismatch, different MFP processors are used ranging from diffraction-limited linear spatial correlators (eq. 2) robust to environmental mismatch to non-linear high-resolution methods that rely on the estimation of $K^{-1}(\omega)$ and are very sensitive to environmental uncertainties (Capon 1969; Widrow & Stearns 1985). The minimum–variance distorsionless processor (MV) is one of these maximum likelihood methods for which the replica vector is modified as follows:

$$\tilde{d}_{\mathrm{MV}}(\omega, a) = \frac{K^{-1}(\omega)\tilde{d}(\omega, a)}{\tilde{d}^{*}(\omega, a) K^{-1}(\omega) \tilde{d}(\omega, a)}, \tag{4}$$

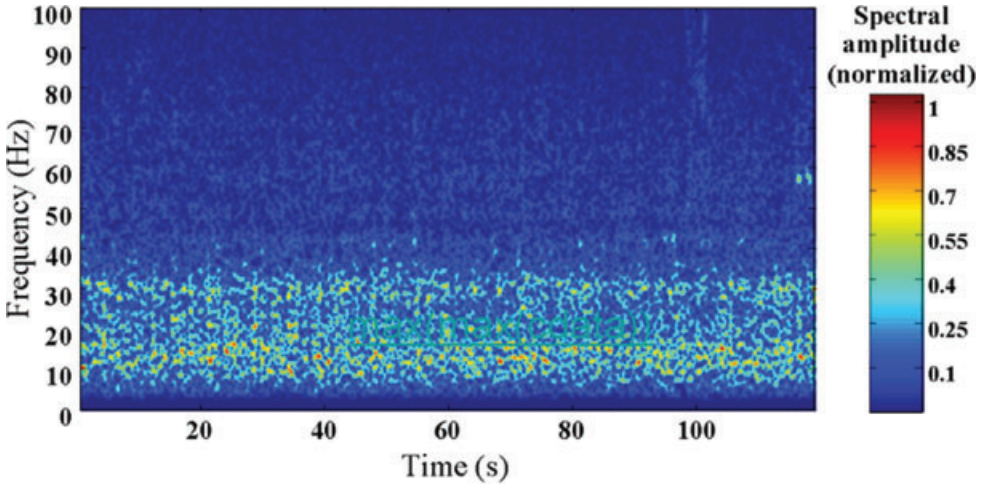

Figure 3. Spectrogram (temporal variations of the spectral density) of the ambient seismic noise recorded during 2 min on station 10, at the east of the network.

which results in the processor output

$$B_{\mathrm{MV}}(a) = \sum_{\omega} |\tilde{d}^{*}_{\mathrm{MV}}(\omega, a) K(\omega) \tilde{d}_{\mathrm{MV}}(\omega, a)| = \sum_{\omega} \frac{1}{|\tilde{d}^{*}(\omega, a) K^{-1}(\omega) \tilde{d}(\omega, a)|}. \quad (5)$$

Jensen *et al.* (1994) show that a small speed mismatch is sufficient to degrade the resolution of MV by introducing sidelobes in the processor output. Actually, two criteria make it possible to assess the quality of an inversion: (1) focusing defined as the accuracy of the spot size and (2) contrast determined by the occurrence of sidelobes, which can introduce an ambiguity on the source location. Jensen *et al.* (1994) showed that this quality was strongly conditioned by the linear or non-linear processor applied on the replica. In many cases, the non-linear procedure (MV) appears more efficient in focussing, but its sensitivity to speed mismatch makes its use more difficult. The white noise constraint processor (WNC), chosen in this study, provides a compromise between resolution and robustness (Debever & Kuperman 2007). In this method, the replica vector is

$$\tilde{d}_{\mathrm{WNC}}(\omega, a) = \frac{(K(\omega) + \varepsilon(\omega, a) I)^{-1} \tilde{d}(\omega, a)}{\tilde{d}^{*}(\omega, a) (K(\omega) + \varepsilon(\omega, a) I)^{-1} \tilde{d}(\omega, a)}, \quad (6)$$

where I is the identity matrix and $\varepsilon(\omega, a)$ is a position-dependent parameter that must satisfy the condition $\tilde{d}^{*}_{\mathrm{WNC}}(\omega, a) \tilde{d}_{\mathrm{WNC}}(\omega, a) \leq \delta^{-2}$ for any source candidate a, δ being a user-defined parameter to be set between 0 and 1. Actually, the relationship between ε and δ is complicated and strongly depends on the quality of the data and the complexity of the propagation medium. One may notice though that $\delta = 1$ corresponds to large values of ε and makes the WNC resemble a linear Bartlett processor. As a matter of fact, when ε goes to infinity, then $\tilde{d}_{\mathrm{WNC}}(\omega, a) \approx \tilde{d}(\omega, a)$ and the WNC processor output

$$B_{\mathrm{WNC}}(a) = \sum_{\omega} |\tilde{d}^{*}_{\mathrm{WNC}}(\omega, a) K(\omega) \tilde{d}_{\mathrm{WNC}}(\omega, a)| \quad (7)$$

is similar to eq. (2). On the other hand, $\delta \sim 0$ leads to $\varepsilon = 0$, which implies after eq. 6 that the WNC behaves as the MV processor (eqs 4 and 5) in this case.

In Fig. 4, the WNC processor output was calculated on a 3-D grid with 2-m horizontal and 1-m vertical intervals. The raw data signals have been normalized between all geophones to balance the local coupling between each geophone and the ground. The ambiguity surface clearly reveals the presence of an acoustic source at depth 1.5 m below the seismic array. The resolution of the acoustic spot is $\sim\lambda/2 = 3.5$ m in all directions as expected from the diffraction theory in the case of a source in the vicinity of the array. With such a shallow source, there is no need to consider depth-dependent velocity models. Actually, given the frequency spectrum of the recorded seismic signals (Fig. 3), we chose to perform the WNC processor in the [18–26 Hz] frequency band as a compromise between (1) a better resolution of the matched-field processor at higher frequency and (2) a good contrast when the matched-field processor is averaged over a large bandwidth. We also took into account the fact that spatial coherence and signal-to-noise ratio are degraded at higher frequency. Figs 5c and 6 are, respectively, the horizontal projection of the acoustic spot integrated over the first 5 m in depth and the vertical projection of the spot along the self-potential profile B presented in Fig. 2.

Finally, Fig. 7a shows a frequency-dependent representation of the WNC output. At each frequency between 7 and 27 Hz, we calculated the WNC output B_{WNC} for spatially uniform velocities ranging from 100 to 500 ms^{-1}. The 3-D positions of the beamformer output

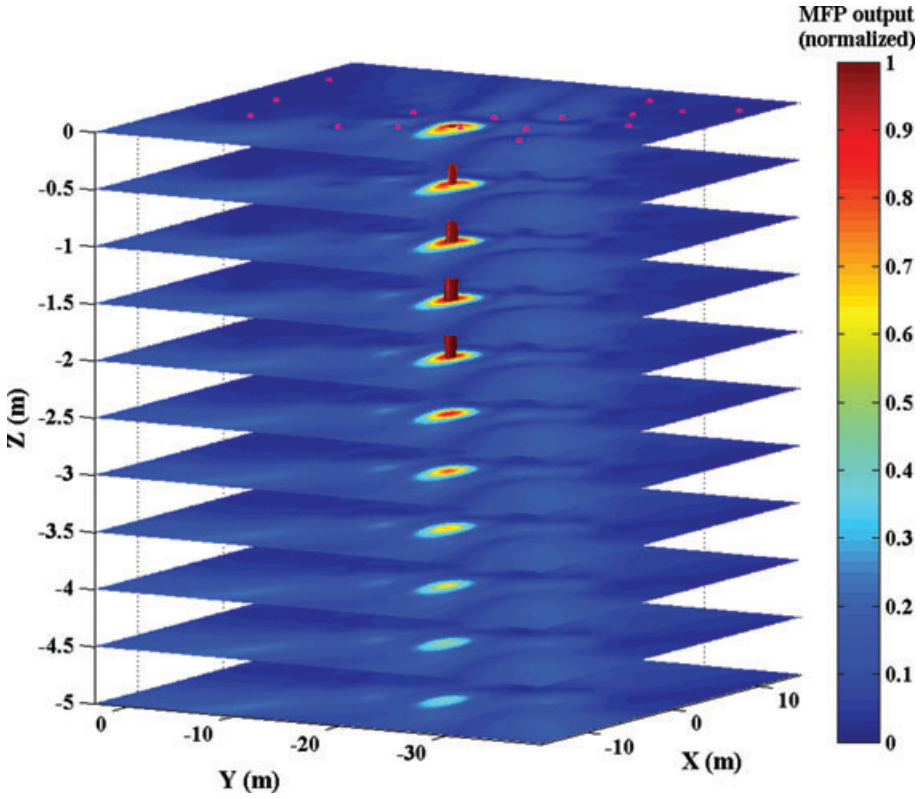

Figure 4. 3-D matched field processing normalized output between 18 and 26 Hz for a homogeneous seismic velocity $c = 160$ ms^{-1}. The coloured surface corresponds to MFP normalized output greater than 0.95. The geophones are indicated as red triangles.

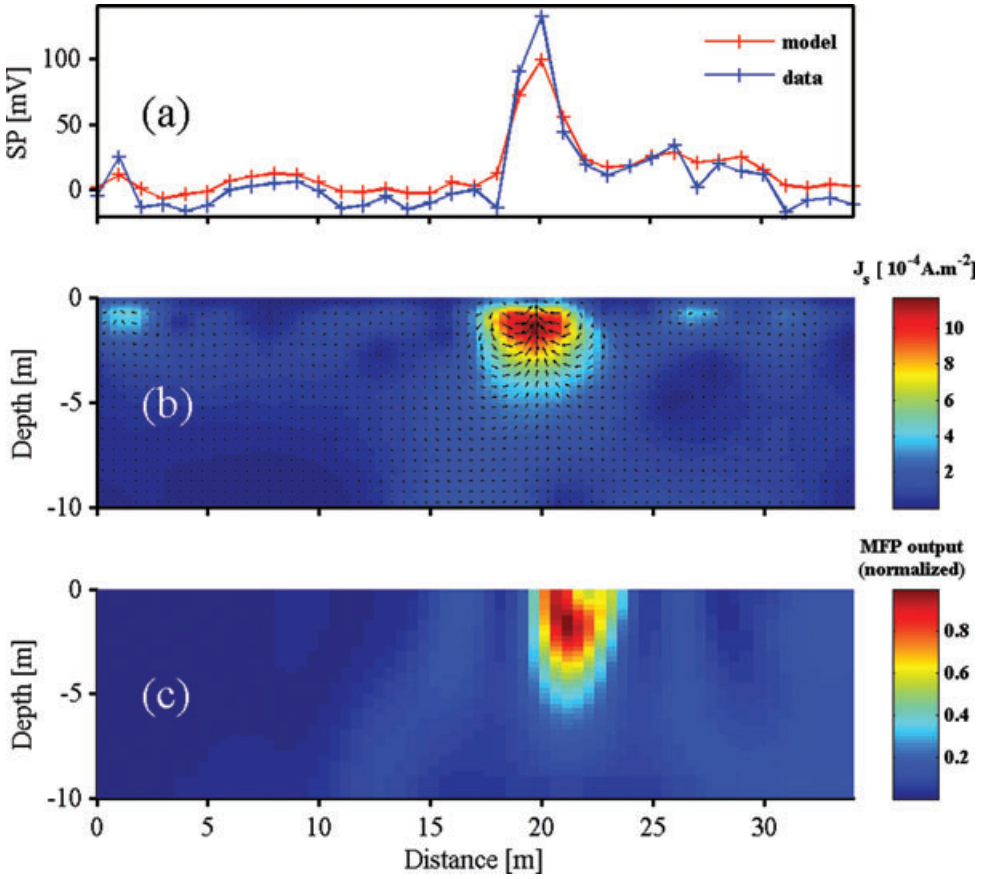

Figure 5. Results of the acoustic and self-potential inversions on the B profile (from B_1 to B_2) shown on Fig. 2. (a) Comparison between the measured self-potential (in blue) with the self-potential (in red) produced by the 2-D model of streaming current density shown below; (b) magnitude of the streaming current density $\vec{j}_s$ obtained by the 2-D inversion method. The arrows indicate the direction of $\vec{j}_s$; (c) vertical cross-section of matched field processing output between 18 and 26 Hz for an homogeneous seismic velocity $c = 160$ ms^{-1}. The results of the inversions show two very close acoustic and electric sources which likely belong to the same hydrothermal structure.

maximum are shown in Figs 7b–d. We observe that the acoustic-source position stays unchanged within the frequency-dependent resolution $\lambda/2$ over the whole frequency bandwidth.

Fig. 7 also shows that, in this particular experimental configuration, seismic waves solve the classical ambiguity in matched-field processing applications between source location and velocity uncertainties. Indeed, both the phase velocity–dispersion curve (Fig. 7a) and the source location (Figs 7b–d) can be simultaneously inverted from ambient noise data. The phase velocity–dispersion curve obtained from the WNC output is also in agreement with phase velocities obtained through active experiments. Of course, such 'source position + velocity' inversion through matched-field processing was made particularly easy in this case thanks to the shallowness of the acoustic source.

2.2 Self-potential method

The self-potential (SP) method aims to measure the electrical potential ψ at the surface of the ground with respect to a fixed reference electrode. Many SP surveys have been conducted in volcanic and geothermal areas (Zablocki 1976; Ishido 2004; Hase *et al.* 2005, for some examples) and have led to a better knowledge of hydrothermal structures and fluid transfer processes. We performed self-potential measurements in the vicinity of the acoustic source with *Petiau* $Pb/PbCl_2$ electrodes and a high impedance (100 MΩ) voltmeter of 0.1 mV sensitivity. SP values vary over the area (Fig. 2) in a 20 mV range except around the acoustic source where we observed a sharp peak of +130 mV slowly decreasing southwards with a small negative anomaly northwards. The northern steaming area, where we can observe hot pools and high surface temperatures, produces neither SP anomaly nor high acoustic energy.

Two major mechanisms are likely to produce self-potential anomalies in hydrothermal areas. The first is the thermo-electric, or Seebeck effect, in which a thermal gradient existing in a geological layer can generate an electric potential. In our case, using a thermo-electric coupling coefficient of 0.2 mV/°C (Corwin & Hoover 1979), a temperature anomaly of 100°C in the shallow sub-surface would give rise to a maximum 20 mV self-potential signal at the surface, that is, about the sixth of the observed signal. This would constitute, if it exists, only a minor contribution to the observed potential. The second polarization mechanism is electrokinetic in nature and called the streaming potential. It is due to the existence of a source current density, called the streaming current density, associated with the flow of water through a porous material (see, e.g. Revil & Leroy 2004). An upward fluid flow is generally recognized as the source of positive self-potential anomalies created by streaming processes above active hydrothermal systems (Ishido & Mizutani 1981; Lénat *et al.* 2000; Zlotnicki & Nishida 2003; Revil *et al.* 2008). In the following, we assume the observed SP anomaly results only from the electrokinetic effects.

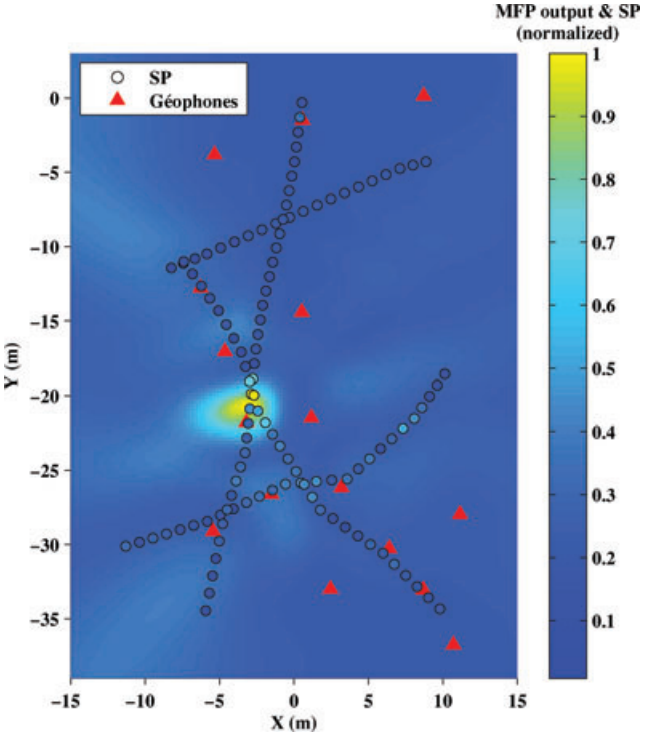

Figure 6. Comparison of the horizontal location of the acoustic source with the self-potential anomaly measured at the surface. The matched field processing output is averaged from 0 to 5 m deep and normalized. The self-potential variations over the area are normalized with reference to the maximum and represented by circles of different colours.

The total electric current density $\vec{j}$(in Am^{-2}) is given by the generalized Ohm's law (Linde *et al.* 2007)

$$\vec{j} = -\sigma\vec{\nabla}(\psi) + \overline{Q_v}\vec{u}, \tag{8}$$

where the first term corresponds to the conduction current density and the second to the streaming current density $\vec{j}_s = \overline{Q_v}\vec{u}$. ψ is the electrical self-potential (in V), σ is the electrical conductivity of the medium (in Sm^{-1}), $\overline{Q_v}$ is the excess of charge of the electric diffuse layer per unit volume of the pore fluid (in Cm^{-3}) and $\vec{u}$ is the Darcy velocity of the pore fluid (in ms^{-1}).

The electrical charge conservation implies

$$\nabla \cdot \vec{j} = 0. \tag{9}$$

Combining eqs (8) and (9) yields a Poisson equation

$$\vec{\nabla} \cdot \sigma\vec{\nabla}(\psi) = \nabla \cdot \vec{j}_s, \tag{10}$$

which governs the streaming potential distribution, the divergence of this streaming current density being responsible for an electric field.

To locate the self-potential source, we have used a 2-D inversion method described in Bolève *et al.* (2009), which is very similar to classical linear inversion methods of potential fields. The forward problem consists in integrating the potential ψ created by a distribution of source current density $\vec{j}_s$ in the medium

$$\psi(M) = \int_\Omega \bar{G}(M, P) \cdot \vec{j}_S(M)\,\mathrm{d}V, \tag{11}$$

where $\bar{G}$ is the Green function connecting the self-potential at a station M at the ground surface produced by streaming density currents at a set of sources P in the conducting source volume Ω. The inverse problem is the minimization of a cost function defined by $\varphi = \|\bar{G}m - d\|$, where $\boldsymbol{m}$ contains the vertical and horizontal components of the streaming current $\vec{j}_s$, and $\boldsymbol{d}$ is the vector containing the self-potential data on the measured 2-D profile.

Because of the lack of high-resolution resistivity measurements, the resistivity is assumed to be homogeneous and equal to 100 Ωm, from the resistivity measurements performed by Legaz *et al.* (2009b) with an electrode spacing of 20 m.

The results of a self-potential inversion (Figs 5 and 6) on the B profile indicate a shallow electric source, of 3–4 m width below the SP peak (Fig. 3), with a predominant vertical component that generates the positive anomaly. From the directions of the streaming current $\vec{j}_s$, we can interpret that there is a small convective shallow structure, most likely fed by the vertical upflow of steam bubbles.

3 DISCUSSION

The position of maximum correlation resulting from the acoustic inversion is very close to the maximum of the streaming current density, indicating the acoustic and electric sources are due to two different processes inside the same localized structure. It is noteworthy that no hydrothermal feature can be seen at the surface above this source, and that the hot steam area with small boiling pools does not produce a high acoustic energy compared to this buried one. The acoustic source location is very shallow, but its depth is not well constrained as the array elevation was not measured due to the dense vegetation. The topography was thus considered as flat whereas the southern part of the array is about 1 m higher than the northern part. The 1 or 2 m distance between the two sources location can be due to the fact that associated physical processes do not occur at the same place in the hydrothermal structure, or results from the heterogeneities in velocity and resistivity on the area.

We suggest the electric source corresponds to the upflow and the convection of boiling fluids at shallow depth below an impermeable layer. The collapse and the merge of steam bubbles as a result of hitting a solid barrier can generate strong acoustic pulses and would correspond to the acoustic source. This solid layer could be made of silica deposited when Old Geyser was active and covered later by deposits from Echo Crater eruptions. The presence of an impermeable layer is in agreement with the low temperatures in the vicinity of the source compared to the northern part. A similar structure of upwelling hydrothermal flow producing a large SP anomaly at the surface was deduced from resistivity, magneto-telluric and self-potential measurements on Mt. Fuji (Aizawa *et al.* 2005), Mt. St. Helens (Bedrosian *et al.* 2007) and Mt. Vulcano (Revil *et al.* 2008).

The lack of self-potential anomaly in the vicinity of the convective structure could be explained by a reduced horizontal water outflow. The thermal energy required to drive the convection can be brought by steam/gas bubbles with a high enthalpy and a corresponding small mass inflow rate. The water mass input and output of the structure would be very small compared to the internal liquid convective flow. Such a model would meet the water flow conservation condition and be in agreement with the observed self-potential and acoustic results. Moreover, in the case of a shallow diffuse horizontal outflow, the likely high water saturation at low depth would increase the electrical conductivity σ and in consequence reduce the self-potential ψ generated at the surface after eq. (10).

4 CONCLUSION

As far as we know, this is the first time acoustic and self-potential methods have been used jointly to give consistent locations of a

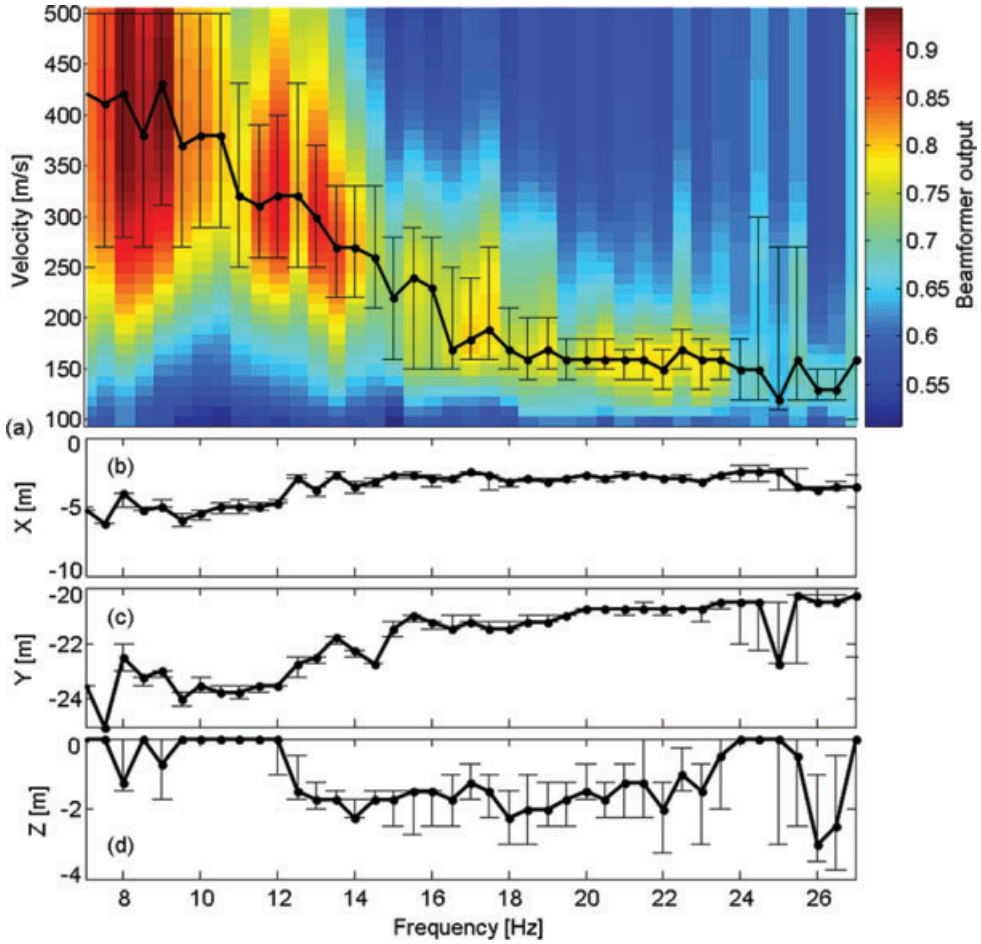

Figure 7. Estimation of velocity model and source location coordinates vs. frequency. (a) Evolution of the WNC beamformer normalized output B_{WNC} in function of the velocity c at a given frequency; the B_{WNC} scale is given by the colour bar. The black circles indicate the velocity for which B_{WNC} is the maximum. Bars correspond to the 95% confidence interval. (b–d) Spatial coordinates X, Y, Z of the maximum $B_{WNC,}$ using the velocity obtained in (a) for this maximum at the given frequency. Bars indicate the range corresponding to the 95% confidence interval in velocity.

unique acoustic and electric buried source produced by subsurface hydrothermal processes. The methods we used were very easy and fast to set up when working at a small scale. We hope to extend this study by a joint electric and acoustic inversion to improve the geometry of the structure and to constrain the fluxes.

A permanent acoustic and self-potential monitoring of this site would give insight on the temporal evolution of the hydrothermal plume, as Tosha *et al.* (1996) has considered this area was also affected by the Inferno cycle. For instance, a 4-D monitoring would investigate the temporal changes in source location and acoustic energy produced, seismic velocity, streaming current and associated groundwater flow. More generally, applying similar techniques to other places, such as an active geyser would improve the understanding of the hydrothermal structures, processes and associated instabilities.

ACKNOWLEDGMENTS

We are grateful to Harvey James of Waimangu Volcanic Valley and the New Zealand Department of Conservation for their assistance.

REFERENCES

Aizawa, K. *et al.,* 2005. Hydrothermal system beneath Mt. Fuji volcano inferred from magnetotellurics and electric self-potential, *Earth planet. Sci. Lett.,* **235,** 343–355.

Almendros, J., Chouet, B. & Dawson P., 2001. Spatial extent of a hydrothermal system at Kilauea volcano, Hawaii, determined from array analyses of shallow long-period seismicity, part I: Method, *J. geophys. Res.,* **106**(B7), 13 565–13 580.

Asten, M.W. & Henstridge, J.D., 1984. Array estimators and use of microseisms for reconnaissance of sedimentary basins, *Geophysics,* **49,** 1828–1837.

Bibby, H., Bennie, S., Stagpoole V. & Caldwell, T., 1994. Resistivity structure of the Waimangu, Waiotapu, Waikite and Reporoa geothermal areas, New Zealand, *Geothermics,* **23,** 445–471.

Bedrosian, P.A., Unsworth, M.J. & Johnston, M.J., 2007. Hydrothermal circulation at Mount St. Helens determined by self-potential measurements, *J. Volc. Geotherm. Res.,* **160,** 137–146.

Bolève, A., Revil, A., Gevaudan, C., Janod, F., Mattiuzzo, J.L. & Fry, J.J., 2009. Preferential fluid flow pathways in embankment dams imaged by self-potential tomography, *Near Surf. Geophys.,* **7**(5–6), 447–462.

Brenguier, F., Shapiro, N.M., Campillo, M., Ferrazzini, V., Duputel, Z., Coutant, O. & Nercessian, A., 2008. Towards forecasting

volcanic eruptions using seismic noise, *Nature Geosci.,* **1,** 126–130, doi: 10.1038/ngeo104.

Bruno, P.P.G., Ricciardi, G.P., Petrillo, Z., Di Fiore, V., Troiano, A. & Chiodini, G., 2007. Geophysical and hydrogeological experiments from a shallow hydrothermal system at Solfatara Volcano, Campi Flegrei, Italy: Response to caldera unrest, *J. Geophys. Res.,* **112,** B06201, doi: 10.1029/2006JB004383.

Capon, J., 1969. High resolution frequency-wavenumber spectrum analysis, *Proc. IEEE,* **57**(8), 1408–1418.

Corwin, R.F. & Hoover, D.B., 1979. The self-potential method in geothermal exploration, *Geophysics,* **44**(2), 226–245.

Debever, C. & Kuperman, W., 2007. Robust matched-field processing using a coherent broadband white noise constraint processor, *J. Acoust. Soc. Am.,* **122,** 1979–1986.

Foti, S., 2000. Multistation methods for geotechnical characterization using Surface waves, *PhD dissertation*. Politecnico di Torino, Italy.

Gouedard, P., Roux, P. & Campillo, M., 2008. Small Scale seismic inversion using surface waves extracted from noise cross-correlation, *J. Acoust. Soc. Am.,* **123**(3), 26–31.

Hase, H., Hashimoto, T., Sakanaka, S., Kanda, W. & Tanaka, Y., 2005. Hydrothermal system beneath Aso volcano as inferred from self-potential mapping and resistivity structure, *J. Volc. Geotherm. Res.,* **143,** 259–277.

Horike, M., 1985. Inversion of phase velocity of long-period microtremors to the S-wave-velocity structure down to the basement in urbanized areas, *J. Phys. Earth,* **33,** 59–96.

Ishido, T., 2004. Electrokinetic mechanism for 'W'-shaped self-potential profile on volcanoes, *Geophys. Res. Lett.,* **31,** L15616, doi: 10.1029/2004GL020409.

Ishido, T. & Mizutani, H., 1981. Experimental and theoretical basis of electrokinetic phenomena in rock-water systems and its applications to geophysics, *J. geophys. Res.,* **86,** 1763–1775.

Jardani, A., Revil, A., Bolève, A. & Dupont, J.P., 2008. Three-dimensional inversion of self-potential data to constrain the pattern of groundwater flow in geothermal fields, *J. geophys. Res.,* **113,** B09204, doi: 10.1029/2007JB005302.

Jensen, F., Kuperman, W., Porter, M. & Schmidt, H., 1994. *Computational Ocean Acoustics,* pp. 578, American Institute of Physics, New York.

Keam, R., 1980. Waimangu, in *Guide to the Geophysics of the Volcanic and Geothermal Area of the North Island of New Zealand, The Royal Society of New Zealand Miscellaneous Series,* N°3, RSNZ, Wellington.

Kieffer, S.W., 1984. Seismicity at Old Faithful Geyser: an isolated source of geothermal noise and possible analogue of volcanic seismicity, *J. Volc. Geotherm. Res.,* **22,** 59–95.

Leet, R.C., 1988. Saturated and subcooled hydrothermal boiling in groundwater flow channels as a source of harmonic tremor, *J. geophys. Res.,* **93**(B5), 4835–4849.

Legaz, A., Revil, A., Roux, P., Vandemeulebrouck, J., Gouedard, P., Hurst, T. & Bolève, A., 2009a. Self-potential and passive seismic monitoring of hydrothermal activity: A case study at Iodine Pool, Waimangu geothermal valley, New Zealand, *J. Volc. Geotherm. Res.,* **179**(1–2), 11–18, doi: 10.1016/j.jvolgeores.2008.09.015.

Legaz, A., Vandemeulebrouck, J., Revil, A., Kemna, A., Hurst, A.W., Reeves, R.R. & Papasin, R., 2009b. A case study of resistivity and self-potential signatures of hydrothermal instabilities, Inferno Crater Lake, Waimangu, New Zealand, *Geophys. Res. Lett.,* **36,** L12306, doi: 10.1029/2009GL037573.

Lénat, J.F., Fitterman, D.V., Jackson, D.B. & Labazuy, P., 2000. Geoelectrical structure of the central zone of Piton de la Fournaise Volcano (Réunion), *Bull. Volcanol.,* **62,** 75–89.

Linde, N., Jougnot, D., Revil, A., Matthaï, S. K., Arora, T., Renard, D. & Doussan C., 2007. Streaming current generation in two-phase flow conditions, *Geophys. Res. Lett.,* **34,** L03306, doi: 10.1029/2006GL028878.

Nairn, I. & Cole, J., 1981. Basalt dikes in the 1886 AD Tarawera rift, *N. Z. J. Geol. Geophys.,* **24,** 585–592.

Revil, A. & Leroy, P., 2004. Governing equations for ionic transport in porous shales, *J. Geophys. Res.,* **109,** B03208, doi: 10.1029/2003JB002755.

Revil, A. *et al*., 2008. Inner structure of La Fossa di Vulcano (Vulcano Island, southern Tyrrhenian Sea, Italy) revealed by high-resolution electric resistivity tomography coupled with self-potential, temperature, and CO2 diffuse degassing measurements, *J. geophys. Res.,* **113,** B07207, doi: 10.1029/2007JB005394.

Roux, P., Sabra, K.G., Gerstoft, P. & Kuperman, W.A., 2005. P-waves from cross-correlation of seismic noise, *Geophys. Res. Lett.,* **32,** L19303.

Shapiro, N.M., Campillo, M., Stehly, L. & Ritzwoller, M.H., 2005. High-resolution surface-wave tomography from ambient seismic noise, *Science,* **29,** 1615–1617.

Scott, B. J., 1994. Cyclic activity in the crater lakes of Waimangu hydrothermal system, New Zealand, *Geothermics,* **23,** 555–572.

Tosha, T., Ishido, T., Nishi, Y., Mastushima, N. & Scott, B., 1996. Seismological and Self-potential surveys at Inferno Crater Lake, Waimangu Geothermal field, *Paper presented at the 18th New Zealand Geothermal Workshop, Geothermal Institute, University of Auckland, Auckland, New Zealand.,* 249–254.

Vandemeulebrouck, J., Stemmelen, D., Hurst, T. & Grangeon, J., 2005. Analogue modeling of instabilities in crater lake hydrothermal systems, *J. geophys. Res.,* **110,** B02212, doi: 10.1029/2003JB002794.

Widrow, B. & Stearns, S., 1985. *Adaptative Signal Processing,* pp. 473, Prentice Hall, Englewood Cliffs, NJ.

Zablocki, C.J., 1976. Mapping thermal anomalies on an active volcano by the self-potential method, Kilauea, Hawaii, in *Proceedings of the Second U.N. Symposium on the Development and Use of Geothermal,* pp. 1299–1309, Resources, San Francisco.

Zlotnicki, J. & Nishida, Y., 2003. Review on morphological insights of self-potential anomalies on volcanoes, *Surveys Geophys.,* **24,** 291–338.

Zywicki, D.J. 1999. Advanced signal processing methods applied to engineering analysis of seismic surface waves, *Ph.D. dissertation*. Georgia Institute of Technology, USA.